nature materials

ARTICLES

https://doi.org/10.1038/s41563-020-00844-w

Activating an adaptive immune response from a hydrogel scaffold imparts regenerative wound healing

Donald R. Griffin[1,2,15], Maani M. Archang[3,15], Chen-Hsiang Kuan[4,5,6,7], Westbrook M. Weaver[3,14], Jason S. Weinstein[8], An Chieh Feng[9], Amber Ruccia[9], Elias Sideris[1], Vasileios Ragkousis[9], Jaekyung Koh[3], Maksim V. Plikus[5,6,10,11], Dino Di Carlo[3], Tatiana Segura[1,12] ✉ and Philip O. Scumpia[9,13] ✉

Microporous annealed particle (MAP) scaffolds are flowable, in situ crosslinked, microporous scaffolds composed of microgel building blocks and were previously shown to accelerate wound healing. To promote more extensive tissue ingrowth before scaffold degradation, we aimed to slow MAP degradation by switching the chirality of the crosslinking peptides from L- to D-amino acids. Unexpectedly, despite showing the predicted slower enzymatic degradation in vitro, D-peptide crosslinked MAP hydrogel (D-MAP) hastened material degradation in vivo and imparted significant tissue regeneration to healed cutaneous wounds, including increased tensile strength and hair neogenesis. MAP scaffolds recruit IL-33 type 2 myeloid cells, which is amplified in the presence of D-peptides. Remarkably, D-MAP elicited significant antigen-specific immunity against the D-chiral peptides, and an intact adaptive immune system was required for the hydrogel-induced skin regeneration. These findings demonstrate that the generation of an adaptive immune response from a biomaterial is sufficient to induce cutaneous regenerative healing despite faster scaffold degradation.

The goal of regenerative medicine is to restore tissue function back to physiological activity. For biomaterial scaffolds, the optimal strategy to achieve this requires balancing material degradation with tissue regrowth. Clinical and patient factors contribute to a wide variation in chemical and physical parameters in situ, which makes striking a degradative–regenerative balance particularly difficult. Our recent development of a flowable, granular biomaterial, that is, a microporous annealed particle (MAP) gel, provides a new approach to make the balance more feasible[1]. The MAP gel is composed of randomly packed microsphere building blocks with a continuous network of interconnected micrometre-scale void spaces that allows for the infiltration of surrounding tissue without the prerequisite of material degradation[1,2]. This unique design resulted in improved tissue closure and improved vascularization relative to a nanoporous (but chemically equivalent formulation) hydrogel in a cutaneous wound model[1].

Mechanical support to the growing tissue by scaffolds is inherently impacted by the degradation rate of the scaffold[3]. For MAP scaffolds, degradation leads to a slow loss of porosity and reduced tissue ingrowth prior to dissolution. We hypothesized that slowing the degradation rate of MAP scaffolds would maintain the porosity and influence both wound closure rate and regenerated tissue quality.

Changing the chirality of peptide moieties leads to a diminished degradation rate by endogenously present enzymes[4,5]. The use of chirality was made more attractive by the fact that polypeptides of D-enantiomeric amino acids do not typically elicit a robust immune response and are considered poorly immunogenic[5]. Previously, we used amino acid chirality to tune the proteolysis rate of peptide nanocapsules for the controlled release of encapsulated growth factors[4]. Therefore, we chose to use an analogous approach to slow the enzymatic degradation of our MAP scaffold by switching the chirality of the peptide crosslinker (for example, L- to D-chirality at the site of matrix metalloprotease (MMP)-mediated bond cleavage). We hypothesized that this approach would maintain the hydrogel microenvironment (for example, charge-based interactions and hydrophobicity) as it increased the long-term hydrogel integrity to allow a full infiltration of cells, and thus provide a greater integration of the entire construct with the host tissue.

In the current study, we investigated how MAP hydrogels crosslinked with either D- or L-amino acid crosslinking peptides affect wound healing and skin regenerative responses using murine wound models. We provide evidence that activation of specific immune responses by the D-amino acid crosslinked MAP hydrogels elicits skin regeneration. Although immunity undoubtedly activates the foreign body response and eventual fibrosis of some implanted

[1]Chemical and Biomolecular Engineering Department, University of California, Los Angeles, CA, USA. [2]Departments of Biomedical Engineering and Chemical Engineering, University of Virginia, Charlottesville, VA, USA. [3]Bioengineering Department, University of California, Los Angeles, CA, USA. [4]Graduate Institute of Clinical Medicine, College of Medicine, National Taiwan University, Taipei, Taiwan. [5]Department of Developmental and Cell Biology, University of California, Irvine, CA, USA. [6]Sue and Bill Gross Stem Cell Research Center, University of California, Irvine, CA, USA. [7]Division of Plastic Surgery, Department of Surgery, National Taiwan University Hospital, Taipei, Taiwan. [8]Department of Medicine and Center for Immunity & Inflammation, Rutgers –New Jersey Medical School, Newark, NJ, USA. [9]Division of Dermatology, Department of Medicine, David Geffen School of Medicine, University of California, Los Angeles, CA, USA. [10]Center for Complex Biological Systems, University of California, Irvine, CA, USA. [11]NSF-Simons Center for Multiscale Cell Fate Research, University of California-Irvine, Irvine, CA, USA. [12]Departments of Biomedical Engineering, Neurology, Dermatology, Duke University, Durham, NC, USA. [13]Department of Dermatology, VA Greater Los Angeles Healthcare System-West Los Angeles, Los Angeles, CA, USA. [14]Present address: Tempo Therapeutics, San Diego, CA, USA. [15]These authors contributed equally: Donald R. Griffin and Maani M. Archang.
✉e-mail: PScumpia@mednet.ucla.edu; Tatiana.segura@duke.edu

biomaterials[6,7], the activation of the correct immune responses may enhance the regenerative ability of a biomaterial[8,9].

D-chiral crosslinker peptides slow MAP degradation in vitro

We first used enantiomeric peptides to change the degradation rate without changing the initial material properties (for example, hydrophobicity, mesh size and charge) of the hydrogel[4]. All amino acids at the site of the enzymatic cleavage for the MMP-degradable peptide were changed to D-amino acids (Ac-GCRDGPQ$_D$GI$_D$W$_D$GQDRCG-NH$_2$, D-peptide). We matched the stiffness (that is, storage modulus) by rheology of both the D-peptide MAP (D-MAP) and L-peptide (L-MAP) formulations to that used in our previous MAP-based cutaneous application (~500 Pa; Fig. 1a). After formulation optimization, we generated the microsphere particles using a previously published microfluidic technique[1]. Following the application of collagenase I to L-MAP, D-MAP or a 50% mixture of D-MAP and L-MAP (1:1 L/D-MAP), the L-MAP hydrogel degraded within minutes, whereas the degradation of the D-MAP by itself or within a mixture with L-MAP was minimal even after one hour (Fig. 1b and Supplementary Fig. 1).

D-chiral crosslinker peptides enhance MAP degradation in vivo

We next examined how D-MAP compares with L-MAP in vivo in a murine splinted excisional wound model[1,10]. We did not find any difference in the wound closure rate or any increased erythema or gross signs of inflammation in wounds treated with D-MAP, L-MAP or a 1:1 mixture of L/D-MAP any time after treatment (days 3 and 6 after wounding are shown in Supplementary Fig. 1a). When comparing wound closure to sham treatment (no hydrogel), we found that a 1:1 mixture of L/D-MAP induced a more rapid wound closure (assessed on day 9 after wounding) than that of sham (Supplementary Fig. 2b), similar to previous results with L-MAP hydrogel[1].

As no differences in wound closure results were noted, we next examined whether the degradation of hydrogels that contained D-amino acid crosslinkers was slowed in vivo by examining excised tissue 21 days after the wound was completely healed. Unexpectedly, histological sections of wounds treated with D-MAP or a 1:1 L/D-MAP hydrogel mixture displayed minimal to no hydrogel persistence 21 days after wounding, near to levels seen in mice not treated with hydrogel (sham), whereas wounds treated with L-MAP hydrogel displayed large amounts of hydrogel remaining (Fig. 1c–f).

D-MAP hydrogels impart tissue regenerative properties

Of note, the initial examination of histological sections of D-MAP and 1:1 L/D-MAP displayed a much different overall appearance than that of the healed sham- or L-MAP-treated wounds. Previous reports suggest that, unlike large excisional wounds in adult mice (wounds larger than 1 × 1 cm), which result in significant regenerative healing with wound-induced hair neogenesis (WIHN)[11–13], wounds smaller than 1 × 1 cm in mice, like the punch biopsies performed in our studies, typically heal without regeneration of new hair and fat and, instead, form scars[12,14,15]. Despite these reports, when the correct regenerative cues are provided from wound fibroblasts, through transgenic activation of specific Hedgehog signals, small wounds can regenerate[16]. Consistent with these results, histological examination of 4 mm excisional splinted wounds in mice that did not receive hydrogel (sham) displayed the typical appearance of scar tissue with a flattened epidermis, a thinned dermis with horizontally oriented collagen bundles, vertically oriented blood vessels and the lack of hair follicles and sebaceous glands (Fig. 1c,g–i). Tissue from mice treated with the L-MAP hydrogel displayed a similar appearance, but with a thicker overall tissue compared with that of sham wounds, due to the substantial residual L-MAP hydrogels (Fig. 1d,g). Within the dermis that surrounds the hydrogel, fibroblasts that secreted collagen and/or extracellular matrix and blood vessels formed between the hydrogel microparticles (Fig. 1d). Only rare hair follicles and associated sebaceous glands were observed in the wound areas (Fig. 1d,h,i). Remarkably, examination of histological sections of the D-MAP- or 1:1 L/D-MAP-treated tissue revealed a de novo regenerated appearance. The overlying epidermis often displayed physiological undulation, and numerous immature-appearing hair follicles were seen to span the length of the healed full-thickness injury (Fig. 1e–i). Samples treated with D-MAP or 1:1 L/D-MAP also displayed an increased skin thickness despite less hydrogel remaining in these samples (Fig. 1f). Many samples also displayed epidermal cyst formation. In samples that displayed residual hydrogel, hair follicles that directly overlaid the degrading MAP hydrogel particles were apparent (Supplementary Fig. 2c). The presence of hair follicles in SKH1 mice was suggestive of embryonic-like tissue regeneration, a phenomenon not often observed in the murine small-wound model.

To further quantify tissue regeneration, we next performed tensile strength testing on unsplinted incisional wounds in SKH1 mice using a modified literature protocol[17]. We found that scar tissue from sham wounds revealed a tensile strength that was approximately 15% of that of unwounded skin from the same animal (Fig. 1i). Although the treatment of wounds with L-MAP hydrogel did not result in a significant increase in tissue tensile strength, treatment with either D- or L/D-MAP resulted in an ~80% improvement in tensile strength (Fig. 1j).

Hair follicles in D-MAP-treated wounds are neogenic

We next repeated wound-healing experiments in C57BL/6 (B6) mice to investigate if the regenerative phenomenon observed in D-MAP treated wounds was similar to that in WIHN. We chose sham as control and D-MAP as a treatment method that showed evidence of regeneration in SKH1 mice. Similar to the sham- and L-MAP-treated wounds in SKH1 mice, the B6 mice wounds without hydrogel (sham) displayed a typical scar appearance with haematoxylin and eosin (H&E) and Masson's trichrome staining (Fig. 2a,c,e). In contrast, histological sections of the D-MAP-treated tissue revealed clear signs of WIHN. As in SKH1 mice, D-MAP-treated B6 mice wounds displayed undulations and numerous epidermal cysts under the epidermis, whereas the dermis was thicker. Importantly, many neogenic hair follicles developed in the wound (Fig. 2b,d,f). The neogenic hair follicles were in the early anagen phases with an immature appearance, yet many of them had already formed new sebaceous glands (Fig. 2b) and featured a prominent SOX9$^+$ bulge stem cell region (Fig. 2j). In several instances, neogenic hair follicles were physically connected to epidermal cysts (a morphology not expected from pre-existing follicles). This suggests that in D-MAP-treated wounds, epidermal cysts can be the initiation sites for de novo morphogenesis for at least some of the neogenic hair follicles (Fig. 2h). Masson's trichrome staining confirmed the presence of neogenic hair follicles within the collagen matrix of the wound bed (Fig. 2b,f). Furthermore, regenerating day 18 D-MAP-treated wounds with neogenic hair follicles lacked PLIN$^+$ dermal adipocytes (Fig. 2h), which is consistent with a slower regeneration of neogenic adipocytes that occurs four weeks after wounding in the large wound-induced WIHN[18,19]. Thus, the addition of D-MAP to normally non-regenerating 4 mm excisional wounds activates hair follicle neogenesis.

D-MAP hydrogel implants enhance myeloid cell recruitment

To determine whether an enhanced immune response led to an enhanced D-MAP or 1:1 L:D-MAP degradation in the wound microenvironment, we utilized a subcutaneous implantation model that also allowed for larger amounts of hydrogel to be implanted, and

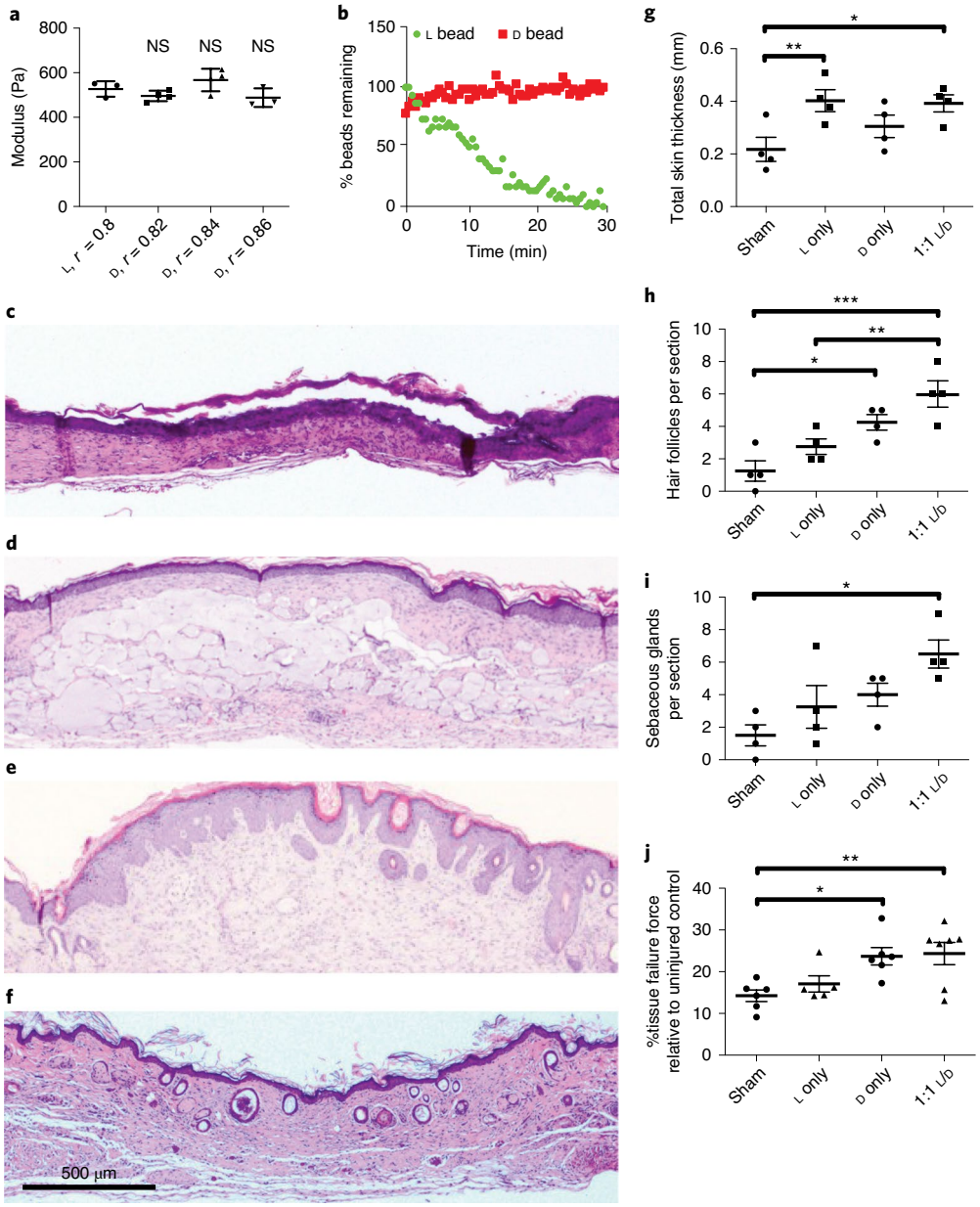

Fig. 1 | D-MAP hydrogel degradation is enhanced in wounds of SKH1 hairless mice. a, Rheological characterization of MAP hydrogels composed of L or D-peptide crosslinked microgels. The *r* ratio (ratio of sulfydryl (SH) to vinyl sulfone (VS)) used to form the microgels was changed to arrive at the same storage modulus for both L- and D-MAP scaffolds. NS, no statistical significance between the L-MAP scaffold to the D-MAP scaffold indicated using a two-tailed Student's *t*-test. **b**, Fabricated L- or D-hydrogels were tested for in vitro enzymolysis behaviour through exposure to a solution of collagenase I (5 U ml^{-1}). **c**–**f**, Representative low-power view of H&E sections from healed skin 21 days after splinted excisional wounding in SKH1 mice treated by from sham (**c**), L-MAP (**d**), D-MAP (**e**) and a 1:1 mixture of L-MAP and D-MAP (**f**). **g**–**i**, Histologic quantification of dermal thickness including gels (**g**) (mm), hair follicles (**h**) and sebaceous glands (**i**). Each point represents the average of two sections from two separate slides of one wound. Each data point represents one animal and all the analysis is by one-way analysis of variance (ANOVA) (F (3,12), 4.448 (**g**), 10.89 (**h**) and 5.074 (**i**); Tukey multiple comparisons tests, $^{*}P = 0.0460$, $^{**}P = 0.0341$ (**g**), $^{*}P = 0.0220$, $^{**}P = 0.0133$, $^{***}P = 0.0007$ (**h**), $^{*}P = 0.0110$ (**i**)). **j**, The incisional, unsplinted wounds were created and, 28 days afterwards, the healed wounds treated without or with the different hydrogels were tested against unwounded skin in the same mouse. The tensile strength was evaluated by tensiometry and reported as a percentage of the tensile strength of the scar tissue when compared with that of the normal skin of the same mouse. Each data point represents the average of two measurements from one wound, separate from wounds used in **b**–**i** with the analysis by one-way ANOVA (F (3, 20), 5.400; $^{*}P = 0.0273$, $^{**}P = 0.0131$). Data are plotted as a scatter plot showing the mean and s.d.

thus remain present for longer than in the small excisional wound model. To test whether the subcutaneous implants of the D-MAP hydrogel resulted in an enhanced immune cell recruitment, we utilized immunofluorescent microscopy with AlexaFluor488-labelled MAP hydrogel. We found that implants that contained only L-MAP displayed a background level of CD11b cells within the hydrogel, as previously observed[1], whereas D-MAP or L/D-MAP resulted in the robust accumulation of CD11b-expressing myeloid cells within and around the scaffold (Fig. 3a,b). A standard histological analysis of a repeat experiment of different formulations of subcutaneously implanted MAP hydrogel confirmed the activation of type 2 immunity with an atypical type 2 granulomatous response dominated

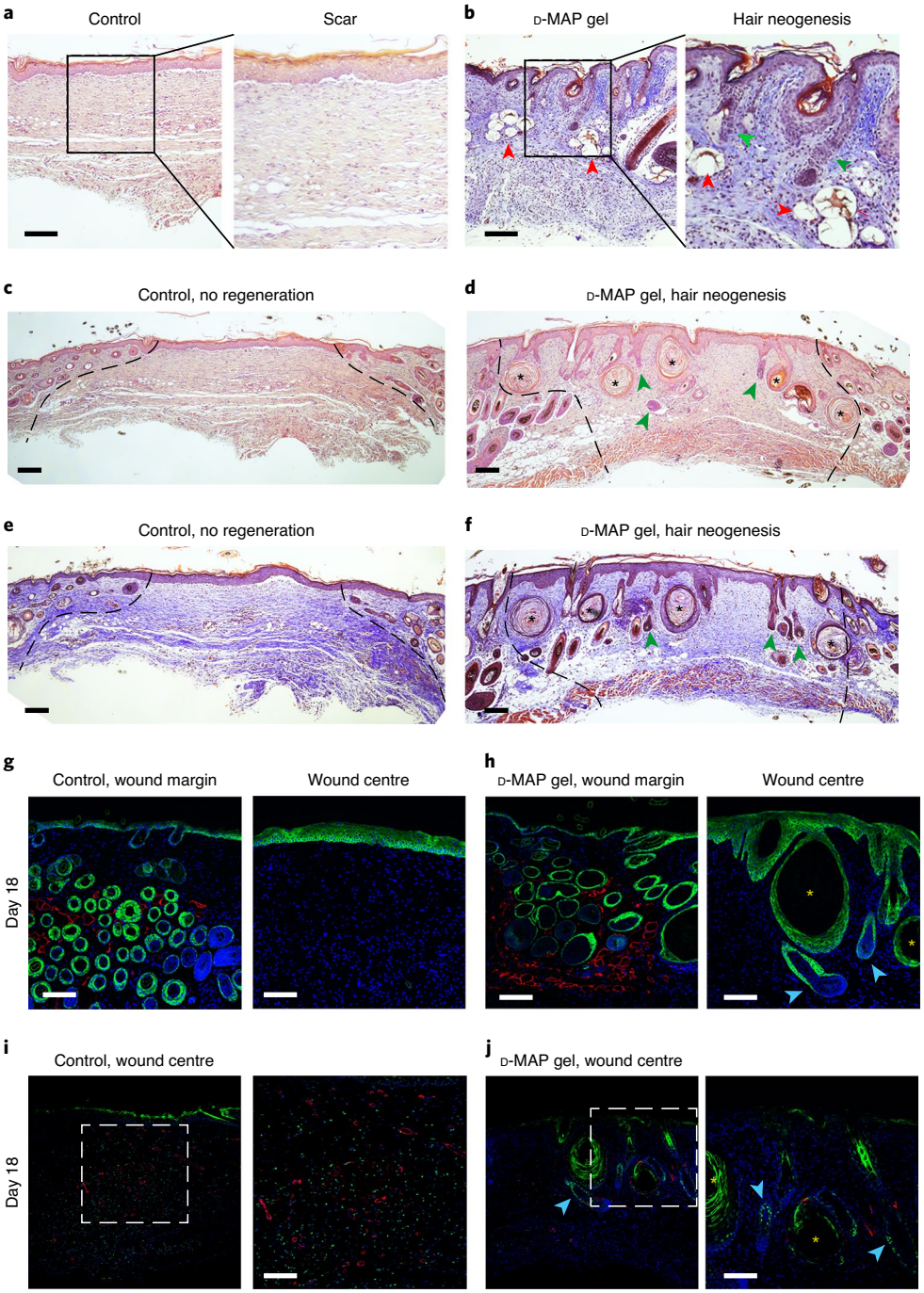

Fig. 2 | D-MAP hydrogel induces neogenesis of hair follicles in full-thickness skin wounds in B6 mice. a–f, H&E (**a**,**c**,**d**) and Masson's trichrome staining (**b**,**e**,**f**) of healed 4 mm full-thickness splinted skin wound on day 18. Control (sham-treated) wounds heal with scarring (**a**,**c**,**e**), whereas D-MAP-treated wounds form numerous epidermal cysts (asterisks) and, prominently, regenerate de novo hair follicles (green arrowheads) (**b**,**d**,**f**). In some instances, neogenic hair follicles form in close association with epidermal cysts. As compared with normal, pre-existing anagen hair follicles at the wound edges, neogenic hair follicles display early anagen stage morphology (the wound edges in **c**–**f** are outlined by dashed lines and the D-MAP hydrogel remnants in **b** are marked with red arrowheads). **g**,**h**, Immunostaining for the epithelial marker KRT5 (green) and the adipocyte marker PLIN (red) reveals normal KRT5$^+$ anagen hair follicles and many mature PLIN$^+$ dermal adipocytes (left panels in **g** and **h**). Regeneration of new KRT5$^+$ hair follicles (blue arrowheads in **h**) along with KRT5$^+$ epidermal cysts (yellow) was observed only in D-MAP-treated wounds (right panels in **g** and **h**). No neogenic adipocytes were observed in hair-forming D-MAP-treated wounds. Blue shows DAPI (4′,6-diamidino-2-phenylindole) staining. **i**,**j**, Immunostaining for SOX9 (green) and SMA (red) reveals many SOX9$^+$ epithelial cells within the bulge region of neogenic hair follicles on day 18 D-MAP-treated wounds (blue arrowheads in **j**). In contrast, in control (sham-treated) wounds that undergo scarring, the dermal wound portion contains many SOX9$^+$ cells, many of which also co-express contractile marker SMA (**i**). Expression of SMA was also seen in both control and D-MAP-treated samples in blood vessels. Scale bars, 100 μm. The images are representative of slides from four animals per group.

by the accumulation of individual macrophages within and around the D-MAP hydrogel implants, but not the L-MAP hydrogel implants (Supplementary Fig. 3a and Supplementary Discussion). Immunofluorescent staining for F4/80 and CD11b confirmed the enhanced recruitment of the macrophages, without giant cell formation, in D-MAP implants (Supplementary Fig. 3b,c and

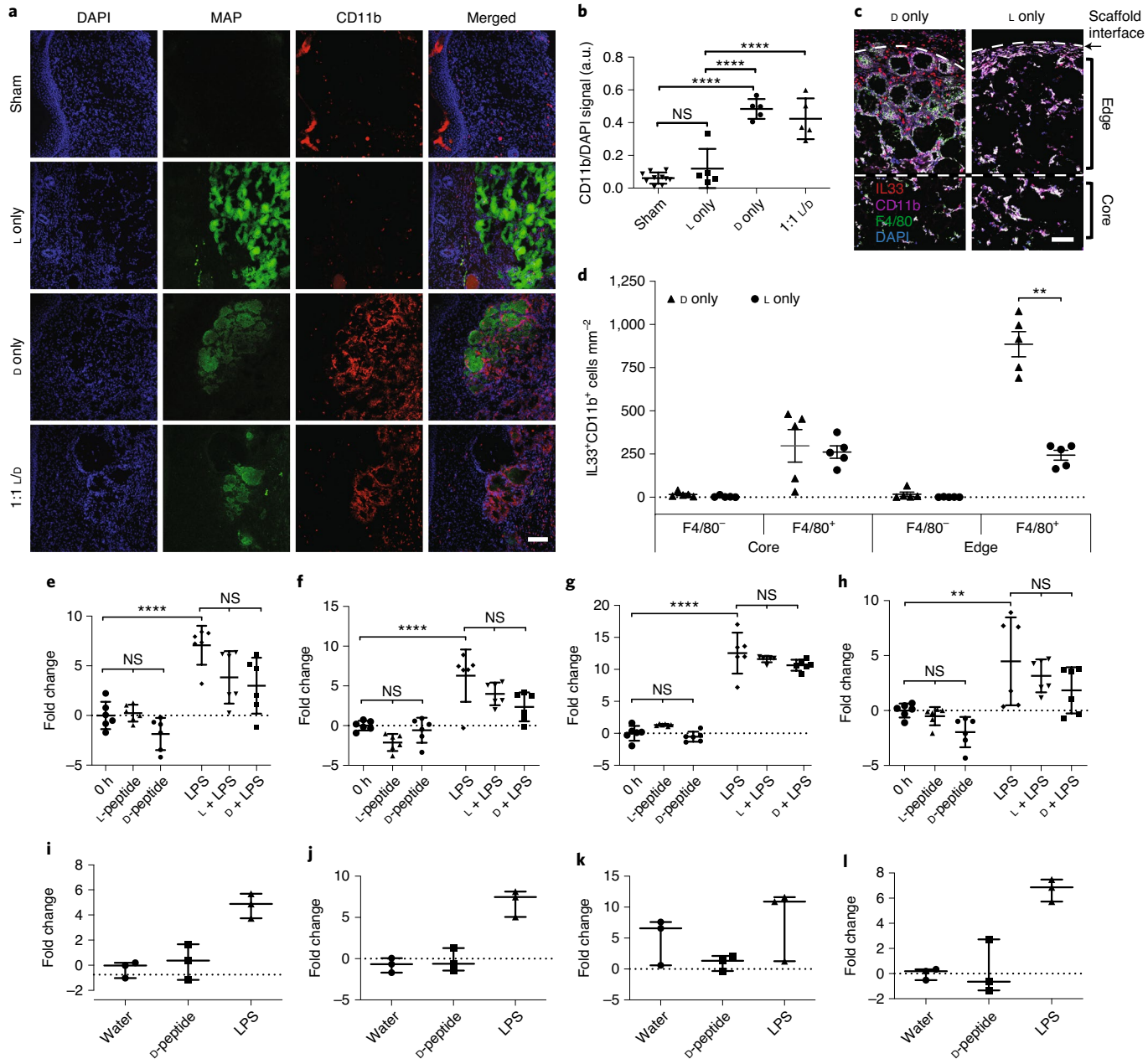

Fig. 3 | Peptide recognition by pattern recognition receptors is not required for myeloid cell recruitment. a, Representative confocal immunofluorescent images of stained myeloid cells (CD11b$^+$) within healed wounds of B6 mice in the presence of the indicated hydrogel. Scale bar, 100 μm. **b**. Localized immune response. Quantification of a CD11b$^+$ cellular infiltrate in healed tissue 21 days after wounding in the presence or absence of a hydrogel. Each point represents average of three slides for each wound. All the analyses are by one-way ANOVA (F (3,21) 41.10; $^{****}P < 0.0001$). **c**,**d**, Representative high-resolution confocal immunofluorescence imaging for CD11b, F4/80, DAPI and IL-33 from subcutaneous implants of L- or D-MAP hydrogel implants (**c**) and quantification of IL-33-producing macrophages and other myeloid cells at the hydrogel edge and core (**d**). $n = 5$ B6 mice, mean ± s.e.m., multiple t-tests adjusted for multiple comparisons using the Holm–Sidak method. $^{**}P = 0.00014$). Scale bar, 100 μm. **e**–**h**, For the uncleaved peptide, murine BMDMs from B6 mice were stimulated with 500 μg ml^{-1} of full-length L- or D-crosslinker peptide in the presence or absence of the LPS (10 ng ml^{-1}) for 6 h. Shown are the quantitative PCR results of four inflammatory genes (*Cxcl1* (**e**), *Tnf* (**f**), *Il1b* (**g**) and *Mx1* (**h**) expression) for two separate experiments performed with $n = 6$. All the analyses are by one-way ANOVA (F (5, 30), 15.66, 17.62, 107.1 and 8.229, respectively; $^{**}P = 0.009$, $^{****}P < 0.0001$). **i**–**l**, For the cleaved peptide, BMDMs were stimulated with LPS (10 ng ml^{-1}) or cleaved D-crosslinker peptide (500 μg ml^{-1}) that possessed an N-terminal D-amino acid (*Cxcl1* (**i**), *Tnf* (**j**), *Il1b* (**k**) and *Mx1* (**l**) expression). The experiment was performed in triplicate. All the analyses are by one-way ANOVA (F (2,6), 20.28, 30.86, 2.178 and 22.72, respectively). Data are plotted as a scatter plot showing the mean and s.d. a.u., arbitrary units.

Supplementary Discussion). These results confirm that D-MAP elicits a more robust immune response and degradation by the accumulated immune cells probably contributed to the enhanced degradation of D-MAP in our previous wound experiments.

Allergic responses and parasites can elicit a type 2 immune response, which includes atypical type 2 granulomatous responses, at least partially through interleukin (IL)-33 production by epithelial cells, recruited myeloid cells and resident macrophages[20–23].

Implanted, non-degradable microparticle-based materials elicit an IL-33-dependent type 2 innate immune response by circulating CD11b$^+$ myeloid cells and macrophages[24]. It is possible that MAP particles could activate this same programme, especially given the atypical type 2 foreign body responses observed in D-MAP samples. Indeed, 21 days after implantation, we found similar numbers of IL-33-expressing F4/80$^+$CD11b$^+$ macrophages in the centre and/or core of both L- and D-MAP implants (Fig. 3c,d), consistent with both L- and D-MAP samples activating this type 2 pathway. However, there was a dramatic increase in IL-33-producing IL-33$^+$F4/80$^+$ macrophages at the edges of the only D-MAP implants (Fig. 3c,d). These results confirm that the hydrogel possesses a type 2 innate 'adjuvant' effect, which may activate the adaptive immune system and contribute to the enhanced immune activation with the D-MAP hydrogel. When L-MAP scaffolds are used, the immune response remains mild as the hydrogel degrades slowly over time[25], but the presence of D-peptide accelerates the immune-mediated degradation.

Free D-chiral peptides avoid pathogen recognition receptors

We next tested whether D-peptides could directly activate innate immunity through a traditional PRR (pattern recognition receptor)-induced transcriptional response. We stimulated murine bone marrow derived macrophages (BMDMs) with L-peptide or D-peptide in the presence or absence of bacterial lipopolysaccharide (LPS), the Toll-like receptor 4 agonist that results in rapid macrophage transcriptional responses. We chose to examine genes reliably and potently induced downstream of the major signalling pathways downstream of a variety of cellular insult (AP-1, MAPK, NF-κB and type I IFN)) to simultaneously interrogate multiple PRR pathways[26–28]. To our surprise, neither L- nor D-amino acid that contained crosslinking peptides alone at high doses (1 mg ml^{-1}) induced the expression of pro-inflammatory genes *Tnf* (NF-κB dependent), *Il1b* (NF-κB and MAPK dependent), *Cxcl2* (AP-1 dependent early response) or *Mx1* (type I IFN dependent) in murine BMDMs at six hours (t_{max} of the gene induction; Fig. 3e–l). Additionally, neither L- nor D-peptides enhanced the ability of LPS to induce the expression of these same genes (Fig. 3e–h).

Previous studies showed that peptides that contain an *N*-terminal D-methionine can activate the innate immune receptor formyl peptide receptor 2 and formyl peptide-like receptor 2[29–31]. As the cleavage of a D-amino acid peptide can result in shorter peptides that contain a D-amino acid at the *N*-terminus, we next wished to examine whether a peptide that corresponded to the cleaved D-peptide could activate inflammatory responses in BMDMs. Similar to the results with the intact D-peptide, a high concentrations of cleaved D-peptide (1 mg ml^{-1}) did not induce the transcription of *Tnf*, *Il1b*, *Cxcl2* or *Mx1* at six hours (Fig. 3i–l). As there is a very low likelihood that the cleaved D-peptide will be present at such high local concentrations within the implanted hydrogel while it is being degraded in vivo, these show that D-chiral peptides are poor activators of a traditional PRR-mediated inflammatory response in macrophages and suggest that D-peptides may act as antigens to enhance immunity, which leads to the enhanced degradation of D-MAP.

D-MAP elicits antigen-specific humoral immunity

We next evaluated whether the D-MAP activated adaptive immunity. The adaptive immune system recognizes non-self-peptide antigens to induce cell mediated (T-cell) and humoral (B-cell) immunity. Peptides that contain D-amino acids were reported to activate or suppress T-cell dependent and T-cell independent adaptive immune responses[5,32]. In the context of the MAP, crosslinking peptides that are non-native may be presented to the immune system until fully degraded. D-peptides could be presented by antigen-presenting cells directly to T cells, which elicits a T-cell dependent adaptive immune response or, alternatively, the presence of D-amino acid-containing peptides on the surface of a large molecule of a MAP hydrogel could directly crosslink the B-cell receptor, which leads to a T-cell independent antibody responses similar to that of T-cell independent antigens. To test this hypothesis, we examined whether mice that were wounded or received subcutaneous implants of L-MAP, D-MAP or 1:1 L/D-MAP were able to develop T-helper cell dependent (IgG1 or IgG2a) or T-cell independent (IgG3) antibodies against L- or D-amino acid-containing crosslinkers[33–36].

Indeed, regardless of whether a D-containing MAP hydrogel was applied to wounded tissue or given via subcutaneous implants, mice developed a T-cell dependent IgG1 and IgG2a response against the D-amino acid-containing peptide, but not a T-cell independent IgG3 response. These results are more consistent with a T cell-dependent immune response against D-peptides (Fig. 4a, b). IgG1 is typically associated with a Th2 'tissue repair' type response, whereas IgG2a is typically associated with a Th1 'foreign body' response that typically requires strong adjuvants to develop, which depend on the strain of the mice[37,38]. The fact that anti-D-peptide-specific IgG2a was induced when the hydrogel was given to mice in a wound environment but not when the hydrogel was given in the subcutaneous implant model suggests that, by itself, the hydrogel does not possess sufficient adjuvant effects to induce robust Th1 responses. However, the inflammation present in the wound environment may result in a mixed Th2/Th1 response to the D-MAP (Figs. 3e and 4b). Mice that were treated with L-MAP alone did not develop antibody responses to the L-peptide.

D-MAP recruits myeloid cells via adaptive immune response

Our data suggest that the activation of adaptive immune responses to D-MAP contributes to the immune infiltration and degradation of D-MAP. To test this hypothesis further, we examined whether Balb/c.Rag2$^{-/-}$γc$^{-/-}$ mice, which are devoid of an adaptive immune system, innate lymphoid cells and IL-2/IL-15 signalling, but possess a fully functional myeloid system, will exhibit a reduced immune infiltration[39]. Indeed, the total cellularity and specific recruitment of CD11b$^+$ myeloid cells to D-MAP hydrogel in Balb/c.Rag2$^{-/-}$γc$^{-/-}$ mice decreased to comparable levels to those seen in L-MAP in wild-type mice (Fig. 4k,l).

D-MAP-induced skin regeneration relies on adaptive immunity

To determine whether the adaptive immune response was required for the development of neogenic hair follicles, we next performed excisional splinted wounds in B6 and B6.Rag1$^{-/-}$ mice and examined them 25 days after wounding with untreated (sham) or treated wounds with the 1:1 L/D-MAP gel. Of note, in preliminary studies scars induced by 4-mm-punch wounds healed with extremely small scars in B6 mice, so we used a 6 mm punch in this experiment.

Sham wounds in B6 mice demonstrated obvious depigmented, irregularly shaped scars, whereas scars in B6 mice treated with 1:1 L/D-MAP gel were difficult to identify visually as they displayed hair growth over the wounds and less atrophy and/or fewer surface changes typically seen in scars (representative example is shown in Fig. 5a, and all the wound images in Supplementary Fig. 4). Scars in sham-treated or 1:1 L/D-MAP-treated B6.Rag1$^{-/-}$ mice were smaller than those in sham-treated B6 mice, but were identifiable in B6.Rag1$^{-/-}$ mice regardless of whether the wounds were sham treated or hydrogel treated (Fig. 5a). All wound areas of the injuries (which included 1:1 L/D-MAP-treated B6 wound areas) were confirmed by examining the defect on the fascial side of the tissue after the excision of skin. Histological sections of the healed skin of mice displayed significant neogenic hairs and sebaceous glands only in wounds of wild-type mice treated with 1:1 L/D-MAP (Fig. 5b–d and Supplementary Fig. 5). Sham wounds in B6 and Rag$^{-/-}$ mice,

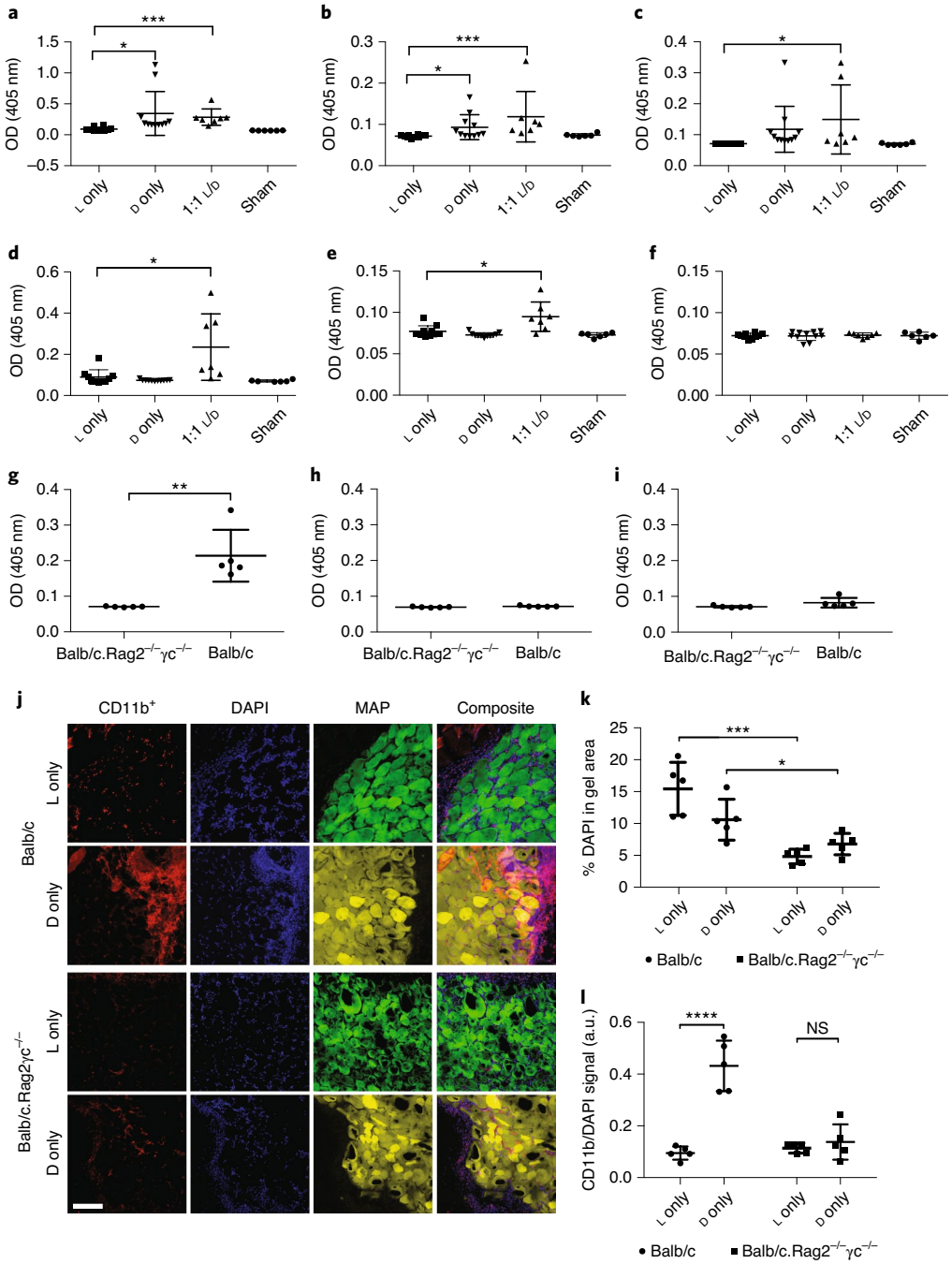

Fig. 4 | D-MAP induces antibody responses and the recruitment of myeloid cells via adaptive immunity. a–f, Wound-healing model. **a–c**, Measurement of anti-d-specific IgG subtype antibodies (anti-d peptide IgG1 (**a**, $^{*}P = 0.0384$, $^{***}P = 0.0004$), anti-d peptide IgG2a (**b**, $^{*}P = 0.0351$, $^{***}P = 0.0262$) and anti-d peptide IgG3 (**c**, $^{*}P = 0.0396$)) by enzyme-linked immunosorbent assay (ELISA) 21 days after the wound healing experiments in SKH1 mice treated with the indicated hydrogels. **d–f**, Measurement of anti-l specific IgG subtype antibodies (anti-l peptide IgG1 (**d**, $^{*}P = 0.0137$), anti-l peptide IgG2a (**e**, $^{*}P = 0.0115$) and anti-l peptide IgG3 (**f**)) by ELISA 21 days after the wound healing experiments in SKH1 mice treated with indicated hydrogels. Each data point represents one animal and all the analyses in **a–f** are by an unpaired two-tailed t-test that compared each condition to l only. **g–i**, Subcutaneous injection model. Measurement of anti-d specific IgG subtype antibodies (anti-d peptide IgG1 (**g**, $^{**}P = 0.0022$), anti-d peptide IgG2a (**h**) and anti-d peptide IgG3 (**i**)) in Balb/c or Balb/c.Rag2−/−γc−/− mice given a subcutaneous injection of d-MAP 21 days after injection. Each data point represents one animal and all the analyses in **g–i** are by an unpaired two-tailed t-test. **j–l**, Representative examples of confocal immunofluorescent imaging for CD11b, DAPI and hydrogel from subcutaneous implants of l- or d-MAP hydrogel implants in Balb/c or Balb/c.Rag2−/−γc−/− mice (**j**), and quantification of total DAPI+ cells (**k**, $^{*}P = 0.0455$, $^{***}P = 0.0006$) and CD11b+ myeloid cells (**l**, $^{****}P < 0.0001$). Scale bar, 200 μm. Data are plotted as a scatter plot showing the mean and s.d. Each point represents the average of three slides for each wound. All the analyses are by an unpaired two-tailed t-test represent statistical significance by Student's t-test for the comparison indicated. OD, outer diameter.

and in the 1:1 L/D-MAP-treated B6.Rag1$^{-/-}$ mice, displayed prominent scars, without hairs or sebaceous glands, which confirms the requirement of an adaptive immune system in skin regeneration by a MAP gel that contains a D-peptide (Fig. 5b–d). These studies highlight that hair follicle structures can be regenerated through adaptive immune activation from MAP hydrogel scaffolds.

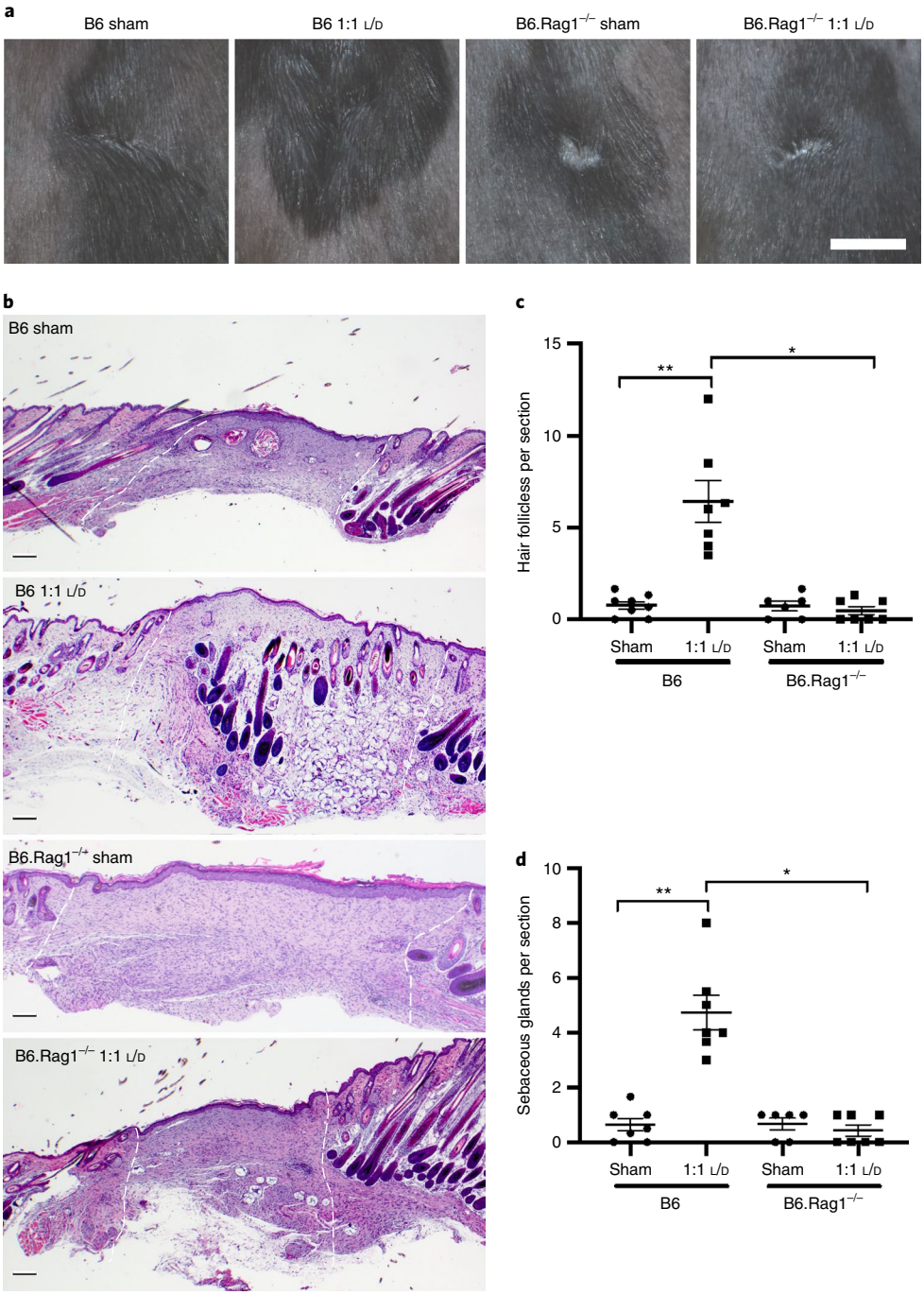

Fig. 5 | D-MAP requires an intact adaptive immunity to induce hair follicle neogenesis. a, Representative examples of gross clinical images of healed splinted excisional wounds in B6 or B6.Rag1$^{-/-}$ mice by a digital single-lens reflex camera 17 days later of sham (no hydrogel) or 1:1 L/D-MAP treatment. Scale bar, 5 mm. **b**, Histologic sections of healed tissue from B6 or B6.Rag1$^{-/-}$ mice. Scale bar, 200 μm. The white dashed lines denote wounded area. **c**,**d**, Quantification of the average numbers of hair follicles (**c**) and sebaceous glands **d**) from three histological sections per sample from B6 mice and B6.Rag1$^{-/-}$ mice. Data are plotted as a scatter plot showing the mean and s.e.m. *Two-tailed $P = 0.002$ by Mann–Whitney test for an interstrain/identical treatment comparison; **$P = 0.0039$ by a Wilcoxon test for an intrastrain/different treatment comparison.

Discussion

In most mammals, the natural process of scar formation and tissue fibrosis is highly evolved and a tissue-scale attempt to restore critical barrier functions for survival. This process, however, is ultimately a biological 'triage' that favours the rapid deposition of a fibrotic matrix to restore the barrier at the expense of a loss of function of complex tissue. In the skin, this fibrotic response results not only in a loss of functioning adnexal structures, but skin tissue that is more fragile and prone to reinjury. A major goal when engineering skin regeneration is to allow for the rapid restoration of barrier function while providing an increased tissue tensile strength and higher tissue function. Many biomaterial-based approaches, which include the addition of growth factors and decellularized extracellular matrix constructs, display limited success in restoring function in wounds. We previously showed that the MAP scaffold can accelerate wound closure in murine wounds[1]. Our findings reported

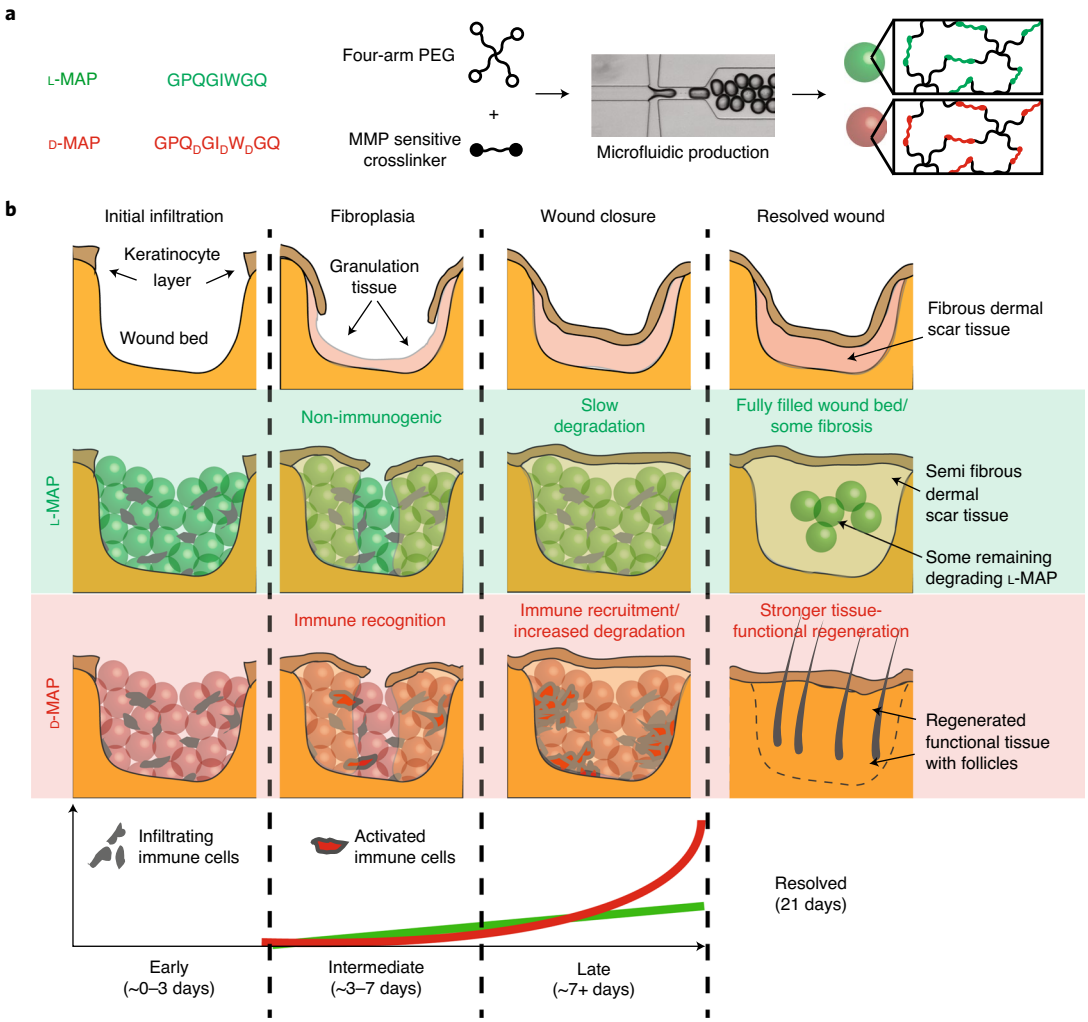

Fig. 6 | D-MAP changes the wound fate from scar formation to regeneration by type 2 immune activation. a, Representation of the MMP cleavage sequences, amino acid chirality within the crosslinking peptides and microfluidic formation of the hydrogel microbeads that incorporate L- or D-chirality peptides. **b**, The use of L- or D-MAP in a wound-healing model demonstrates that both the L-MAP (green) and D-MAP (red) hydrogels fill the wound defect. Wounds that heal in the absence of a hydrogel heal with an atrophic scar and loss of tissue (top row), whereas the epidermis forms over the scaffold with both L- and D-MAP and allows an increased dermal thickness (middle two rows). However, in the case of D-MAP, the hydrogel activates the adaptive immune system over time, which results in tissue remodelling and skin regeneration as the adaptive immune system degrades the D-MAP scaffold (bottom row). PEG, polyethylene glycol.

here further highlight that the incorporation of a modest adaptation of MAP that enhanced a type 2 innate and adaptive immune response induced skin regeneration—hair neogenesis and improved tensile strength (Fig. 6). This response was dependent on the generation of an adaptive immune response to D-enantiomeric peptides and occurred without the addition of stem cells, growth factors or adjuvants. Importantly, this regenerative response was decoupled from wound closure that begins immediately, consistent with the time needed to generate an antigen-specific immune response.

Although adaptive immunity can contribute to fibrosis, foreign body formation and the rejection of biomaterial implants[6–8], adaptive immune activation from a growth factor that contains extracellular matrices can enhance muscle regeneration[8,9]. Further, other biomaterials were created to directly activate specific components of the immune system to treat cancer as immunotherapy platforms[40,41]. In concert, these studies suggest that the role of the adaptive immune system in tissue repair is substantially more complex than previously realized. Our findings suggest that an engineered type 2 immune response to sterile, degradable microparticle-based materials can trigger regeneration rather than fibrosis and further support a role of adaptive immune cells to restore tissue function. Finally, we display the potential of the MAP scaffold as a potent immunomodulatory platform. Future identification of immune factors that tip the balance towards regeneration rather than eliciting scarring or a foreign body response may lead to improved biomaterials.

Online content

Any methods, additional references, Nature Research reporting summaries, source data, extended data, supplementary information, acknowledgements, peer review information; details of author contributions and competing interests; and statements of data and code availability are available at https://doi.org/10.1038/s41563-020-00844-w.

Received: 5 March 2019; Accepted: 25 September 2020;
Published online: 09 November 2020

References

1. Griffin, D. R., Weaver, W. M., Scumpia, P., Di Carlo, D. & Segura, T. Accelerated wound healing by injectable microporous gel scaffolds assembled from annealed building blocks. *Nat. Mater.* **14**, 737–744 (2015).
2. Nih, L. R., Sideris, E., Carmichael, S. T. & Segura, T. Injection of microporous annealing particle (MAP) hydrogels in the stroke cavity reduces gliosis and inflammation and promotes NPC migration to the lesion. *Adv. Mater.* **29**, 1606471 (2017).
3. Xu, Q. et al. Injectable hyperbranched poly(β-amino ester) hydrogels with on-demand degradation profiles to match wound healing processes. *Chem. Sci.* **9**, 2179–2187 (2018).
4. Zhu, S., Nih, L., Carmichael, S. T., Lu, Y. & Segura, T. Enzyme-responsive delivery of multiple proteins with spatiotemporal control. *Adv. Mater.* **27**, 3620–3625 (2015).
5. Sela, M. & Zisman, E. Different roles of D-amino acids in immune phenomena. *FASEB J.* **11**, 449–456 (1997).
6. Doloff, J. C. et al. Colony stimulating factor-1 receptor is a central component of the foreign body response to biomaterial implants in rodents and non-human primates. *Nat. Mater.* **16**, 671–680 (2017).
7. Mishra, P. K. et al. Sterile particle-induced inflammation is mediated by macrophages releasing IL-33 through a Bruton's tyrosine kinase-dependent pathway. *Nat. Mater.* **18**, 289–297 (2019).
8. Chung, L., Maestas, D. R., Housseau, F. & Elisseeff, J. H. Key players in the immune response to biomaterial scaffolds for regenerative medicine. *Adv. Drug Deliv. Rev.* **114**, 184–192 (2017).
9. Sadtler, K. et al. Developing a pro-regenerative biomaterial scaffold microenvironment requires T helper 2 cells. *Science* **352**, 366–370 (2016).
10. Galiano, R. D., Michaels, J., Dobryansky, M., Levine, J. P. & Gurtner, G. C. Quantitative and reproducible murine model of excisional wound healing. *Wound Repair Regen* **12**, 485–492 (2004).
11. Ito, M. et al. Wnt-dependent de novo hair follicle regeneration in adult mouse skin after wounding. *Nature* **447**, 316–320 (2007).
12. Seifert, A. W. et al. Skin shedding and tissue regeneration in African spiny mice (*Acomys*). *Nature* **489**, 561–565 (2012).
13. Nelson, A. M. et al. dsRNA released by tissue damage activates TLR3 to drive skin regeneration. *Cell Stem Cell* **17**, 139–151 (2015).
14. Guerrero-Juarez, C. F. et al. Wound regeneration deficit in rats correlates with low morphogenetic potential and distinct transcriptome profile of epidermis. *J. Invest. Dermatol.* **138**, 1409–1419 (2018).
15. Marshall, C. D. et al. Sanativo wound healing product does not accelerate reepithelialization in a mouse cutaneous wound healing model. *Plast. Reconstr. Surg.* **139**, 343–352 (2017).
16. Lim, C. H. et al. Hedgehog stimulates hair follicle neogenesis by creating inductive dermis during murine skin wound healing. *Nat. Commun.* **9**, 4903 (2018).
17. Carlson, M. A. & Chakkalakal, D. Tensile properties of the murine ventral vertical midline incision. *PLoS ONE* **6**, e24212 (2011).
18. Plikus, M. V. et al. Regeneration of fat cells from myofibroblasts during wound healing. *Science* **355**, 748–752 (2017).
19. Guerrero-Juarez, C. F. et al. Single-cell analysis reveals fibroblast heterogeneity and myeloid-derived adipocyte progenitors in murine skin wounds. *Nat. Commun.* **10**, 650 (2019).
20. Warren, K. S. A functional classification of granulomatous inflammation. *Ann. NY Acad. Sci.* **278**, 7–18 (1976).
21. Chensue, S. W. et al. Cytokine responses during mycobacterial and schistosomal antigen-induced pulmonary granuloma formation. Production of Th1 and Th2 cytokines and relative contribution of tumor necrosis factor. *Am. J. Pathol.* **145**, 1105–1113 (1994).
22. Wills-Karp, M. et al. Trefoil factor 2 rapidly induces interleukin 33 to promote type 2 immunity during allergic asthma and hookworm infection. *J. Exp. Med.* **209**, 607–622 (2012).
23. Hardman, C. S., Panova, V. & McKenzie, A. N. J. IL-33 citrine reporter mice reveal the temporal and spatial expression of IL-33 during allergic lung inflammation. *Eur. J. Immunol.* **43**, 488–498 (2013).
24. de Kouchkovsky, D. A., Ghosh, S. & Rothlin, C. V. Induction of sterile type 2 inflammation. *Nat. Mater.* **18**, 193–194 (2019).
25. Koh, J. et al. Enhanced in vivo delivery of stem cells using microporous annealed particle scaffolds. *Small* **15**, e1903147 (2019).
26. Purbey, P. K. et al. Defined sensing mechanisms and signaling pathways contribute to the global inflammatory gene expression output elicited by ionizing radiation. *Immunity* **47**, 421–434 (2017).
27. Scumpia, P. O. et al. Opposing roles of Toll-like receptor and cytosolic DNA-STING signaling pathways for *Staphylococcus aureus* cutaneous host defense. *PLoS Pathog.* **13**, e1006496 (2017).
28. Tong, A.-J. et al. A stringent systems approach uncovers gene-specific mechanisms regulating inflammation. *Cell* **165**, 165–179 (2016).
29. Kim, S. D. et al. The agonists of formyl peptide receptors prevent development of severe sepsis after microbial infection. *J. Immunol.* **185**, 4302–4310 (2010).
30. Kang, H. K. et al. The synthetic peptide Trp-Lys-Tyr-Met-Val-D-Met inhibits human monocyte-derived dendritic cell maturation via formyl peptide receptor and formyl peptide receptor-like 2. *J. Immunol.* **175**, 685–692 (2005).
31. Schepetkin, I. A. et al. 3-(1 *H*-indol-3-yl)-2-[3-(4-nitrophenyl)ureido] propanamide enantiomers with human formyl-peptide receptor agonist activity: molecular modeling of chiral recognition by FPR2. *Biochem. Pharmacol.* **85**, 404–416 (2013).
32. Zisman, E., Dayan, M., Sela, M. & Mozes, E. Ia-antigen–T-cell interactions for a thymus-independent antigen composed of D amino acids. *Proc. Natl Acad. Sci. USA* **90**, 994–998 (1993).
33. Cernysiov, V., Gerasimcik, N., Mauricas, M. & Girkontaite, I. Regulation of T-cell-independent and T-cell-dependent antibody production by circadian rhythm and melatonin. *Int. Immunol.* **22**, 25–34 (2010).
34. Honda, S. et al. Enhanced humoral immune responses against T-independent antigens in Fc alpha/muR-deficient mice. *Proc. Natl Acad. Sci. USA* **106**, 11230–11235 (2009).
35. Mongini, P. K., Stein, K. E. & Paul, W. E. T cell regulation of IgG subclass antibody production in response to T-independent antigens. *J. Exp. Med.* **153**, 1–12 (1981).
36. Weinstein, J. S. et al. Maintenance of anti-Sm/RNP autoantibody production by plasma cells residing in ectopic lymphoid tissue and bone marrow memory B cells. *J. Immunol.* **190**, 3916–3927 (2013).
37. Germann, T. et al. Interleukin-12 profoundly up-regulates the synthesis of antigen-specific complement-fixing IgG2a, IgG2b and IgG3 antibody subclasses in vivo. *Eur. J. Immunol.* **25**, 823–829 (1995).
38. Boehler, R. M., Graham, J. G. & Shea, L. D. Tissue engineering tools for modulation of the immune response. *BioTechniques* **51**, 239–254 (2011).
39. Song, J. et al. A mouse model for the human pathogen *Salmonella typhi*. *Cell Host Microbe* **8**, 369–376 (2010).
40. Park, C. G. et al. Extended release of perioperative immunotherapy prevents tumor recurrence and eliminates metastases. *Sci. Transl. Med.* **10**, eaar1916 (2018).
41. Kim, J. et al. Injectable, spontaneously assembling, inorganic scaffolds modulate immune cells in vivo and increase vaccine efficacy. *Nat. Biotechnol.* **33**, 64–72 (2015).

Methods

L-MMP and D-MMP MAP hydrogel formation. Microfluidic water-in-oil droplet generators were fabricated using soft lithography, as previously described[1]. To enable the microgel formation, two aqueous solutions were prepared. One solution contained a 10% w/v four-arm polyethylene glycol–vinyl sulfone (20 kDa, JenKem) in 300 mM triethanolamine (Sigma), pH 8.25, prefunctionalized with a 500 μM K-peptide (Ac-FKGGERCG-NH_2) (GenScript), 500 μM Q-peptide (AcNQEQVSPLGGERCG-NH_2) and 1 mM RGD (Ac-RGDSPGERCG-NH_2) (GenScript). The other solution contained either: (1) an 8 mM dicysteine-modified MMP substrate (Ac-GCRDGPQGIWGQDRCG-NH_2) (GenScript) with either all L-chirality amino acid residues for L-MMP microgel, or (2) D-chirality amino acid substitution of amino acids at the site of the MMP-mediated recognition and cleavage (Ac-GCRDGPQ_DGI$_D$W$_D$GQDRCG-NH_2) for D-MMP microgels. We matched the stiffness of the two hydrogels that required minimal changes to that of the peptide crosslinker solution (L-MAP, 8 mM; D-MAP, 8.2 mM). The oil phase was a heavy mineral oil (Fisher) that contained 0.25% v/v Span-80 (Sigma). The two solutions were mixed in the droplet generator and pinched immediately into monodisperse droplets. Downstream of the pinching region, a second oil inlet with a high concentration of Span-80 (5% v/v) was mixed with the flowing droplet emulsion. Both aqueous solution flow rates used were 0.75 μl min^{-1}, whereas both oil solutions flowed at 4 μl min^{-1}. The mixture was allowed to react overnight at room temperature and purified by repeated washes with an aqueous buffer of HEPES-buffered saline pH 7.4 and pelleting in a tabletop centrifuge at 18,000*g* for 5 min. Raw materials were purchased endotoxin free and the final hydrogels were tested for endotoxin levels prior to implantation.

Generation of MAP scaffolds from building block microgels. Fully swollen and equilibrated building block microgels were pelleted at 18,000*g* for 5 min and the excess buffer (HEPES pH 7.4 + 10 mM $CaCl_2$) was removed by aspiration. Subsequently, building blocks were split into aliquots, each of which contained 50 μl of the concentrated building blocks. An equal volume of HEPES pH 7.4 + 10 mM $CaCl_2$ was added to the concentrated building block solutions. Half of these are spiked with thrombin (Sigma) to a final concentration of 2 U ml^{-1} and the other half were spiked with FXIII (CSL Behring) to a final concentration of 10 U ml^{-1}. These solutions were then well mixed and spun down at 18,000*g*, followed by the removal of excess liquid with a cleanroom wipe (American Cleanstat).

Annealing was initiated by mixing equal volumes of the building block solutions that contained thrombin and FXIII using a positive displacement pipette (Gilson). These solutions were well mixed by pipetting up and down, repeatedly, in conjunction with stirring using the pipette tip. The mixed solution was then pipetted into the desired location (mould, well plate, mouse wound and so on) or loaded into a syringe for subcutaneous injection. The microgel fabrication was performed under sterile conditions. After particle fabrication, 20 μl of dry particles were digested in 200 μl of digestion solution (Collagenase IV 200 U ml^{-1} + DNase I 125 U ml^{-1}) and incubated in 37 °C for 30 min before testing. Endotoxin concentrations were determined with the Pierce LAL Chromogenic Endotoxin Quantitation Kit (Thermo Fisher Scientific) following the manufacturer's instructions. Particle endotoxin levels were consistently below 0.2 endotoxin U ml^{-1}.

Degradation with collagenase. Microgel degradability was confirmed with collagenase I. A 1:1 v/v mixture of microgels formed with D-MMP- or L-MMP-sensitive crosslinker was diluted in collagenase I to a final concentration of 5 U ml^{-1} collagenase. This mixture was added to 1 mm polydimethylsiloxane well and briefly allowed to settle. Images of the microgels were taken near the bottom of the well every 30 s for 2 h with a confocal microscope. Image analysis was carried out through a custom MATLAB script (script provided by S. C. Lesher-Perez) and ImageJ. MATLAB was used to determine the number of intact microgel spheres in each image. The previously mentioned script was applied with a minimum droplet radius of 30 pixels, a maximum droplet radius of 50 pixels and a sensitivity factor of 0.98 for the channel-separated images. Then, ImageJ was used to determine the area fraction that fluoresced for each channel and each image. The thresholding for each image was set to a minimum of 50 and a maximum of 255 and the fluorescing area fraction was recorded.

Mouse excisional wound-healing model. All the experiments that involved animals, animal cells or tissues were performed in accordance with the Chancellor's Animal Research Committee ethical guidelines at the University of California Los Angeles under protocol no. 10-011 (in vivo wound healing and subcutaneous implants) or no. 1999-073 (in vitro BMDM cultures). Mouse excisional wound healing experiments were performed as previously described[1,10]. Briefly, 10-week-old female SKH1 mice (n = 6, Charles River Laboratories) or 10-week-old female B6 or B6.Rag1$^{-/-}$ mice (n = 4 twice, Jackson Laboratories) were anaesthetized using a continuous application of aerosolized isoflurane (1.5 vol%) throughout the duration of the procedure and disinfected with serial washes of povidone–iodine and 70% ethanol. The nails were trimmed and buprenorphine (0.05 mg ml^{-1}) was injected intramuscularly. The mice were placed on their side and the dorsal skin was pinched along the midline. A sterile 4 mm biopsy punch was then used to create two through-and-through wounds, which resulted in four clean-cut, symmetrical, full-thickness excisional wounds on either side of the dorsal midline. A small amount of adhesive (VetBond, 3M, Inc.) was then applied to one side of a rubber splint (outer diameter, ~12 mm; outer diameter, ~8 mm) and the splint was placed centred around the wound (adhesive side down). The splint was secured with eight interrupted sutures of 5-0 non-absorbable Prolene. A second splint wrapped in Tegaderm (3M, Inc.) was attached to the initial splint via a single suture to act as a hinged cover to allow wound imaging while it acted as a physical barrier above the wound bed. After the addition of thrombin (2 U ml^{-1}) and 10 mM $CaCl_2$, the experimental material (20 μl of L-only MAP, D-only MAP or a 1:1 v/v mixture of L-MAP and D-MAP in HEPES-buffered saline that contained factor XIII (10 U ml^{-1}) and 10 mM $CaCl_2$, or no hydrogel) was then added to one of the wound beds randomly to ensure each hydrogel treatment was applied to the different regions of wounded back skin to limit the potential for site-specific effects. After treatment, a Tegaderm-coated splint was applied and wound sites were covered using a self-adhering elastic bandage (VetWrap, 3M, Inc.). Animals were housed individually to prevent wound manipulation. At the culmination of the wound-healing experiment (day 21 or day 25), the mice were killed by an isoflurane overdose and cervical dislocation and imaged with a digital camera. The skin was excised and processed via either paraffin embedding for H&E or optimal cutting temperature blocks for immunofluorescence.

Evaluation of wound closure. Wounds were imaged daily to follow their closure. Each wound site was imaged using a high-resolution camera (Nikon Coolpix). The closure fraction was determined as described previously[1]. Briefly, closure was determined by comparing the pixel area of the wound to the pixel area within the 10 mm centre hole of the red rubber splint. Closure fractions were normalized to day 0 for each mouse and/or scaffold sample. Investigators were blinded to the treatment group identity during analysis.

Wound imaging. On the specified day after the wounds were created, close-up images of the wounds were taken using a Canon Powershot A2600 or a Nikon D3400 DSLR Camera with an 18–55 mm lens, and were cropped to the wound area but not manipulated further. For wound closure, the area was obtained using ImageJ by a subject blinded to the treatment.

Tissue collection. After the wounds healed, mice were killed on the indicated day after wounding, and tissue collected with a ~5 mm margin around the healed wound. The samples were immediately submerged in Tissue-Tek optimal cutting temperature fluid and frozen into a solid block with liquid nitrogen. The blocks were then cryosectioned by a cryostat microtome (Leica) and kept frozen until use. The sections were then fixed with 4% paraformaldehyde in 1× PBS for 30 min at room temperature, washed with 1× PBS and kept at 4 °C until stained. For the antibody production analysis, was blood harvested via cardiac puncture to obtain the serum for ELISA.

Macrophage cell culture. Mouse BMDMs were generated as previously described previously[27]. Briefly, after euthanasia, the hindlimbs were removed aseptically and the bone marrow was flushed. Bone marrow cells were cultured in CMG-conditioned complete DMEM media for 6 days. Cells were then treated with intact L- or D-peptide in ultrapure H_2O at the indicated concentration in the presence or absence of LPS (10 ng ml^{-1}). Cleaved D-peptide (with an N-terminal D-amino acid) (W_DGQDRCG-NH_2) was also used when indicated. Cells were harvested at 6 h after treatment and the expression of cytokines and chemokines was examined by quantitative PCR using specific primers, as described previously[42].

Incisional wound model. As above, 10-week-old female B6 mice (Jackson Laboratories) were anaesthetized with isoflurane as above. The dorsal and side skin was dehaired using electric clippers followed by Nair (Church and Dwight, Inc.), then disinfected with serial washes of povidone–iodine and 70% ethanol. The nails were trimmed to lower the incidence of splint removal, and buprenorphine was injected intramuscular as above. An incisional 2 cm × 1 cm wound was made with a scalpel. Mice (five per group) were randomly assigned to receive 50 μl of L-MAP, D-MAP, 1:1 v/v mixture of L-MAP and D-MAP or no hydrogel (Aquaphor, Beiersdorf Inc.). The mice were wrapped with Tegaderm followed by VetWrap, as above.

Histology and analysis. Samples were sectioned (6–10 μm thick), then stained with H&E or Masson trichrome by the UCLA Tissue Procurement Core Laboratory using standard procedures. Sections were examined by a board-certified dermatopathologist (P.O.S.) and/or an expert in hair follicle neogenesis/regeneration (M.V.P.) who were blinded to the identity of the samples for the presence of adnexal structures in tissue sections and dermal thickness. For enumeration, two to three tissue sections from the tissue block of each wound were examined and averaged per wound to obtain the count per unit area for each sample. Wounds were splinted to prevent contraction and any sample with more than a 50% wound closure by contraction were not included.

Tensiometry. To evaluate the tensile properties of the healed incisional wounds, tensile testing was performed on an Instron model 3342 fitted with a 50 N load

cell and data recorded using the Instron Bluehill 3 software package. Tissue was collected from the wound site 28 days after wounding and treatment as a 2 cm × 4 cm 'dumbbell' shape (with a 1 cm centre width in the handle portion). The sample was oriented such that the healed wound spanned the entire middle section of the dog bone (the thinner 1 cm region) and the healed wound long axis was orthogonal to the direction of tension applied. The tissue sample was loaded into the Instron and secured with pneumatic grippers, pressurized to 276 kPa. The tissue was subjected to tensile testing at an elongation rate of 5 mm min^{-1} and ran through material failure.

For each tissue sample, stress/strain curves were calculated from force/elongation curves (provided from the Instron Bluehill software) using the known cross-sectional dimensions of the 'dog bone' samples (each measured with callipers prior to placement on the Instron), and by measuring the starting distance between pneumatic grips with a caliper. The starting distance was standardized by preloading the sample to 0.5 N, followed by measurement and then running of the tensile test to failure. This analysis enabled the calculation of yield stress, which are reported in Fig. 1j.

Subcutaneous implants of hydrogel. For subcutaneous implants, after anaesthesia, 10-week-old female Balb/c and Balb/c.Rag2$^{-/-}\gamma c^{-/-}$ mice were injected with 50 µl of L-MAP, D-MAP or 1:1 v/v mixture of L-MAP and D-MAP ($n=5$). After 21 days, the skin and subcutaneous tissue that contained the hydrogels were removed and processed for histology and immunofluorescence, and blood was collected by cardiac puncture to obtain serum for the ELISA. B6 mice were used in another batch of experiments for immunofluorescence analysis and the histology of subcutaneous implants.

Tissue section immunofluorescence, quantification of hydrogel degradation and immune infiltration. Slides that contained tissue sections (10–25 µm thickness) were blocked with 3% normal goat serum (NGS) in 1× PBS + 0.05% Tween-20 (PBST). For intracellular antigens, 0.2% triton was added to the blocking buffer. Primary antibody dilutions were prepared in 5% NGS in 1× PBST as follows: rat anti-mouse CD11b clone M1-70 (BD Pharmingen, no. 553308) 1:100, F4/80 clone A3-1 (BioRAD, MCA497G) 1:400 and IL-33 (Abcam, ab187060) 1:200. Sections were stained with primary antibodies overnight at 4 °C, and subsequently washed with 3% NGS in 1× PBST. Secondary antibodies (goat anti-rat Alexa-647; Invitrogen) were all prepared in 5% NGS in 1× PBST at a dilution of 1:500. Three 5 min washes with PBST were performed after each antibody incubation. Sections were incubated in secondary antibodies for 1 h at room temperature and subsequently washed with 1× PBST. For multicolour immunofluorescence staining for primary and secondary antibodies of each antigen were performed in sequence. Sections were either mounted with antifade mounting medium with DAPI (Fisher Scientific, H1200) or counterstained with 2 µg ml^{-1} DAPI in 1× PBST for 30 min at room temperature and then mounted in mounting medium of Antifade Gold.

Computational analysis of multicolour immunofluorescence images. A MATLAB code was used for the analysis of the multicolour immunofluorescence images. The code divided the hydrogel into an edge region (300 µm from hydrogel–tissue interface) and a core region (the centre of the hydrogel to 200 µm from the inner boundary of the edge region). For each hydrogel subregion, the code read the CD11b and F4/80 signals, and binarized each to form a mask using a similar threshold for all the samples. The code then used the nuclear stain and IL-33$^+$ stains to identify all the nuclei and IL-33$^+$ cells. The density of each cell type was then quantified by counting the number of nuclei and IL-33$^+$ cells that overlapped or evaded the masks divided by the area of the region of interest. Areas with defects caused by tissue sectioning were excluded from the analysis. Although it did not affect the code performance, the image condition was kept the same across all samples.

ELISA. To assess the anti-L- or anti-D-antibodies, sera were collected by cardiac puncture 21 days after the hydrogel application of mice (subcutaneous implant or application to wound). To detect the anti-L- and anti-D-antibodies, plates were coated with either the L-MMP or D-MMP peptide, respectively (the sequence above; GenScript). Serum samples were tested at a 1:500 dilution followed by incubation with alkaline phosphatase-labelled goat anti-mouse IgG1 or IgG2a, or IgG3 antibodies (Southern Biotechnology Associates or BD Pharmingen) and developed with *p*-nitrophenyl phosphate substrate (Sigma-Aldrich). The optical density at 405 nm was read using a Spectramax i3X microplate reader (Softmax Pro 3.1 software; Molecular Devices).

Statistics and reproducibility. All the statistical analysis was performed using Prism 6 (GraphPad, Inc.) software. Specifically, a two-tailed *t*-test or one-way ANOVA were used to determine the statistical significance, assuming an equal sample variance for each experimental group when individual groups are compared. For ANOVA, post hoc analysis with Tukey multiple comparison was used. For histological counting and the B6 and B6.Rag1$^{-/-}$ sham versus 1:1 L/D-MAP analysis, a Wilcoxon signed rank analysis was performed and for B6 versus B6.Rag1$^{-/-}$ the subcutaneous immunofluorescence analysis was performed with a *t*-test with a Mann–Whitney U test.

The hydrogel degradation test was performed on three separate occasions for each batch of L-MAP, D-MAP and 50:50 mixture of L-MAP and D-MAP for a total of nine degradation tests. In each technical replicate at least ten microgels were imaged and analysed for fluorescence intensity.

The evaluation of hair neogenesis in the B6 mice control versus D-MAP for Fig. 2 was performed on samples from $n=4$ for each group. The wound healing studies to compare wild-type to B6.Rag1$^{-/-}$ mice were repeated three times ($n=4$ each group). In the first experiment, all the Rag1-/- mice were euthanized due to the development of severe and worsening wound infections, and thus were not included in the final analysis. In addition, wounds and/or scars that showed more than a 50% contraction of the wound area from the underlying fascia from any group or histological processing results that failed to identify the wound and/or scar bed (that is, the sample was cut through) were removed from the final dataset. For the histological analysis, sham versus 1:1 L/D-MAP in B6 mice from three separate experiments were used ($n=9$ histological samples available out of an available $n=12$ wounds performed), whereas samples in the B6.Rag1$^{-/-}$ mice were obtained from the latter two experiments performed in B6 versus B6.Rag1$^{-/-}$ mice carried out at the same time ($n=6$ histological samples available out of $n=8$ wounds). The findings within this article were observed in two different mouse strains (CRL-SKH and C57BL/6) that have different adnexal structures (vellus hair only and mature and/or terminal follicles, respectively).

Reporting summary. Further information on research design is available in the Nature Research Reporting Summary linked to this article.

Data availability

The data that support the findings of this study are available from the corresponding authors upon reasonable request. Source data are provided with this paper.

References

42. Ramirez-Carrozzi, V. R. et al. A unifying model for the selective regulation of inducible transcription by CpG islands and nucleosome remodeling. *Cell* **138**, 114–128 (2009).

Acknowledgements

We thank the National Institutes of Health F32EB018713-01A1 (D.R.G.), T32-GM008042 (M.M.A.), T32AR071307 (M.M.A), U01AR073159 (M.V.P.), R01NS094599 (T.S.), R01HL110592 (T.S.), R03AR073940 (P.O.S.), K08AR066545 (P.O.S.), Pew Charitable Trust (M.V.P.), LEO Foundation (M.V.P.), the National Science Foundation grant DMS1763272, Simons Foundation Grant (594598, QN) (M.V.P.), and the Presidential Early Career Award for Scientists and Engineers (N00014-16-1-2997) (D.D.) for funding. We thank S. C. Lesher-Perez and M. Bogumil for their assistance with MATLAB coding. We thank Y. Liu for assistance with running the endotoxin texts. We also thank the Advanced Light Microscopy and Spectroscopy at California NanoSystems Institute and Electron Microscopy Core Laboratory of the Brain Research Institute at UCLA and, particularly, for the significant help of M. Cilluffo.

Author contributions

D.R.G., P.O.S. and T.S. conceived the experiments. D.R.G., W.M.W., E.S., M.M.A. and J.K. carried out the microfluidic design and fabrication, and D.D.C. oversaw the microfluidic design and fabrication. D.R.G., M.M.A., C.-H.K., W.M.W, J.S.W., A.C.F., E.S., A.R., V.R. and P.O.S. performed the experiments. D.R.G., M.M.A., J.S.W., A.R., M.V.P., T.S. and P.O.S. analysed and interpreted the data. D.R.G., M.M.A., P.O.S. and T.S. wrote the manuscript and all the authors discussed the results and contributed to writing portions of the manuscript and editing the manuscript. D.R.G. and M.M.A. contributed equally to this work. The co-principal investigators are P.O.S. and T.S.

Competing interests

D.R.G., W.M.W., D.D.C., T.S., and P.O.S. have a financial interest in Tempo Therapeutics, which aims to commercialize MAP technology.

Additional information

Supplementary information is available for this paper at https://doi.org/10.1038/s41563-020-00844-w.

Correspondence and requests for materials should be addressed to T.S. or P.O.S.

Reprints and permissions information is available at www.nature.com/reprints.

nature research

Corresponding author(s): Tatiana Segura Philip Scumpia

Last updated by author(s): May 29, 2020

Reporting Summary

Nature Research wishes to improve the reproducibility of the work that we publish. This form provides structure for consistency and transparency in reporting. For further information on Nature Research policies, see Authors & Referees and the Editorial Policy Checklist.

Statistics

For all statistical analyses, confirm that the following items are present in the figure legend, table legend, main text, or Methods section.

n/a	Confirmed	
☐	☒	The exact sample size (*n*) for each experimental group/condition, given as a discrete number and unit of measurement
☐	☒	A statement on whether measurements were taken from distinct samples or whether the same sample was measured repeatedly
☐	☒	The statistical test(s) used AND whether they are one- or two-sided *Only common tests should be described solely by name; describe more complex techniques in the Methods section.*
☐	☒	A description of all covariates tested
☐	☒	A description of any assumptions or corrections, such as tests of normality and adjustment for multiple comparisons
☐	☒	A full description of the statistical parameters including central tendency (e.g. means) or other basic estimates (e.g. regression coefficient) AND variation (e.g. standard deviation) or associated estimates of uncertainty (e.g. confidence intervals)
☐	☒	For null hypothesis testing, the test statistic (e.g. *F*, *t*, *r*) with confidence intervals, effect sizes, degrees of freedom and *P* value noted *Give P values as exact values whenever suitable.*
☒	☐	For Bayesian analysis, information on the choice of priors and Markov chain Monte Carlo settings
☒	☐	For hierarchical and complex designs, identification of the appropriate level for tests and full reporting of outcomes
☒	☐	Estimates of effect sizes (e.g. Cohen's *d*, Pearson's *r*), indicating how they were calculated

Our web collection on statistics for biologists contains articles on many of the points above.

Software and code

Policy information about availability of computer code

Data collection	MATLAB 2017b was used to quantify particle degradation for Figure 1a as a function of change in fluorescent signal with time. ImageJ 1.52a was used to determine pixel surface area measurements for wound closure quantification for Figure 3a-b. For Figure 3c-d MATLAB R2019a was used to count cells by identifying nuclei and assigning them to different cell types based on overlab with other signals.
Data analysis	Prism (v6) was used for completion of all t-test and ANOVA statistical analyses.

For manuscripts utilizing custom algorithms or software that are central to the research but not yet described in published literature, software must be made available to editors/reviewers. We strongly encourage code deposition in a community repository (e.g. GitHub). See the Nature Research guidelines for submitting code & software for further information.

Data

Policy information about availability of data

All manuscripts must include a data availability statement. This statement should provide the following information, where applicable:

- Accession codes, unique identifiers, or web links for publicly available datasets
- A list of figures that have associated raw data
- A description of any restrictions on data availability

The data that support the findings of this study are available from the corresponding authors upon reasonable request.

Field-specific reporting

Please select the one below that is the best fit for your research. If you are not sure, read the appropriate sections before making your selection.

☒ Life sciences ☐ Behavioural & social sciences ☐ Ecological, evolutionary & environmental sciences

For a reference copy of the document with all sections, see nature.com/documents/nr-reporting-summary-flat.pdf

Life sciences study design

All studies must disclose on these points even when the disclosure is negative.

Sample size	The minimum wound healing animal group sample size was for the CRL-SKH mice (n = 6), which was determined based on previous published results for this material platform (Griffin et al. Nature Materials 2015). The other wound healing study, WT vs Rag1, (n = 4, twice) was chosen due to limitations in knock out mouse availability. For comprison of different gel formulations in B6 mice, n = 6 or 8 was chosen to control for multiple comparisons. The subcutaneous injections (n = 5) was chosen due to an expectation for lower variability associated with a non-open wound application.
Data exclusions	No data was excluded from analysis
Replication	The wound healing study comparing WT to Rag1 was repeated twice. The findings of this paper were also confirmed by observing the same regenerative effects in two different mouse strains (CRL-SKH and WT/C57Bl/6) that have different adnexal structures (vellus hair only and mature/terminal follicles, respectively).
Randomization	For the WT to Rag1 comparison, the first experiment was all control on right and for the second the control was on the left. As control and treatment were on the same mice no further randomization was necessary. For the CRL-SKH wound healing study the group placement was completely randomized between L, D, L/D, and sham.
Blinding	The dermatopathologist was blinded for histopathologic interpretation and quantification, however the presence of hydrogel prevented some samples from being considered as negative controls (sham). Gel degradation, immunofluorescence, qPCR and ELISA automatically by the relevant softwares and devices and did not require blinding. The troubleshooting of scripts was performed with a delabelled images.

Reporting for specific materials, systems and methods

We require information from authors about some types of materials, experimental systems and methods used in many studies. Here, indicate whether each material, system or method listed is relevant to your study. If you are not sure if a list item applies to your research, read the appropriate section before selecting a response.

Materials & experimental systems

n/a	Involved in the study
☐	☒ Antibodies
☒	☐ Eukaryotic cell lines
☒	☐ Palaeontology
☐	☒ Animals and other organisms
☒	☐ Human research participants
☒	☐ Clinical data

Methods

n/a	Involved in the study
☒	☐ ChIP-seq
☒	☐ Flow cytometry
☒	☐ MRI-based neuroimaging

Antibodies

Antibodies used	Rat anti mouse CD11b clone M1-70 (BD Pharmingen; #553308); Rat anti mouse F4/80 clone A3-1 (BioRAD; MCA497G); Rabbit anti mouse IL-33 (abcam; ab187060); Goat anti-rat Alexa-647 (Invitrogen, # A-21247); Goat anti-rat Alexa-488 (Invitrogen, # A-11006); Goat anti-rabbit Alexa-568 (Invitrogen, # A-11011), alkaline phosphatase-labeled goat anti-mouse IgG1 or IgG2a, or IgG3 antibodies (Southern Biotechnology Associates #1070-04 and #1100-04, and BD Pharmingen #553389 all at 1:2000).
Validation	The Rat anti-mouse CD11b and F4:80 antibodies have been used across multiple publications, including for immunofluorescent labeling of frozen sections as used here (J Immunol. 1981 Jan;126(1):359-64; J Leukoc Biol. 1996 May;59(5):648-55; Cell Mol Biol. 2019 Sep;12:339-413; Bioeng Transl Med. 2016 Jul;1(2)136–148). The Rabbit anti-mouse IL33 was validated for IF on frozen section by abcam and used across multiple publications (Cell Mol Biol Lett. 2018 Oct;23,52;J Cell Cycle. 2019 Nov;18(23)3393-403). The Goat anti-rat and rabbit antibodies have been used across multiple publications, including for immunofluorescent staining of frozen sections as used here (Methods Mol Biol. 2017;1560:179-188. doi: 10.1007/978-1-4939-6788-9_12; Neoplasia. 2016 Dec;18(12):732-741. doi: 10.1016/j.neo.2016.10.001; J Clin Invest. 2014 Aug;124(8):3325-38. doi: 10.1172/JCI73932; Sci Rep. 2016 Jun;6:28238). All antibodies were further tested in frozen sections of spleen for validation and adjustment of concentration.

Animals and other organisms

Policy information about studies involving animals; ARRIVE guidelines recommended for reporting animal research

Laboratory animals	10 week old female mice of the following species were used: CRL-SKHhrhr (Charles River); C57Bl/6 (Jackson Laboratories); Rag1-/- (Jackson Laboratories); Rag2-/- gamma c-/- (Radiation Oncology Breeding Colony at UCLA; Balb/c background); Balb/c (Radiation Oncology Breeding Colony at UCL
Wild animals	Study did not involve wild animals.
Field-collected samples	Study did not involve samples collected from the field.
Ethics oversight	All experiments involving animals, animal cells or tissues were performed in accordance to the Chancelor's Animal Research Committee (ARC) ethical guidelines at UCLA under protocol # 10-011 (in vivo wound healing and subcutaneous implants) or # 1999-073 (in vitro BMDM cultures).

Note that full information on the approval of the study protocol must also be provided in the manuscript.